

Supplementary Materials for
**Light-induced protein structural dynamics in bacteriophytochrome revealed
by time-resolved x-ray solution scattering**

Sang Jin Lee *et al.*

Corresponding author: Xiaojing Yang, xiaojing@uic.edu; Hyotcherl Ihee, hyotcherl.ihee@kaist.ac.kr

Sci. Adv. **8**, eabm6278 (2022)
DOI: 10.1126/sciadv.abm6278

This PDF file includes:

Supplementary Methods
Supplementary Discussions
Figs. S1 to S10

Supplementary Methods

Elimination of the solvent heating contribution from time-resolved difference scattering curves

Time-resolved difference scattering curves contain not only the contribution of changes in protein structure but also the contribution from the heating of the solvent by the energy transferred from the excited protein molecules. Using a well-established method, the contribution of the solvent heating response was reconstructed as a linear combination of the X-ray scattering change due to the temperature change at a constant pressure and that due to the density change at a constant temperature and was removed from the TRXSS data to extract only the contributions related to the structural changes of the target protein molecules (ref. 55-57 of the main text). Heating-free difference scattering curves were obtained by subtracting the scaled solvent heating signal from the difference scattering curves for PaBphP at the positive time delays.

Measurement and analysis of static X-ray scattering data

Static X-ray scattering data and TRXSS data were collected at the 14-ID-B beamline at the Advanced Photon Source (APS) according to the established experimental protocol (ref. 55-57 of the main text). Prior to starting the TRXSS measurement, we carried out static X-ray solution scattering measurements on the solution sample of PaBphP-PCM under dark-adapted and illuminated conditions at room temperature (fig. S3, B and C). The dark-adapted state was achieved by incubating the protein sample in the dark for 30 min. By flowing the protein sample stored in the dark-incubated condition, ten consecutive scattering curves were collected, where each curve was measured with an exposure time of 3 sec. Next, we illuminated the protein sample for 20 min prior to X-ray exposure. By flowing the protein sample kept in the illuminated condition, ten consecutive scattering curves were collected under the exact same condition to the dark-incubated measurement. These measurements, implemented in dark-incubated and illuminated conditions, were repeated twice. As a result, a total of 40 curves in four sets were collected, with two dark sets and two light sets in alternating order (fig. S3C). In addition, we collected one control set including ten consecutive scattering curves of the neat buffer to check the level of background noise (fig. S3C). From the measured static scattering curves, we built a $n_q \times n_i$ matrix A_{static} , where n_q is the number of q -points in a given scattering curve and n_i is the number of the scattering curves with i denoting the index of the scattering curves. For the data presented in this paper, n_q and n_i were 119 and 50, respectively. Subsequently, a singular value decomposition (SVD) analysis was applied to A_{static} to obtain the static difference between the dark-adapted and illuminated states, as shown in fig. S3B. In this procedure, the data matrix is decomposed into three matrices: U , S , and V , where U is a matrix in which the columns called the left singular vectors (LSVs) are composed of index-independent q spectra, V is a matrix in which the columns called the right singular vectors (RSVs) are composed of index-dependent amplitude changes of the LSVs, and S is a matrix whose diagonal elements are the weights of the singular vectors. From the SVD analysis, the most significant LSV (LSV1), attributed to the light-induced structural changes between the dark and illuminated states, was obtained, as shown in fig. S3B. To check the reversibility of the photoconversion of PaBphP, we also obtained the most significant RSV (RSV1), including the amplitude changes of LSV1, as a function of the index of the static scattering curves (fig. S3C). During the entire measurement, the diluted protein solution with a concentration of 5 mg/ml continuously flowed into a capillary-based cell at a rate of 12 $\mu\text{l}/\text{sec}$ to alleviate the unwanted effects from X-ray radiation damage.

Size-exclusion chromatography

The elution profiles for the dark and illuminated states of PaBphP were measured using size-exclusion chromatography (SEC). To obtain the elution profile for the dark-adapted condition, the purified protein sample (5 mg/ml; 500 ml) pre-incubated in the dark on ice for ~30 min was loaded onto a SEC column (Superdex 6 Increase 10/300 GL) covered with aluminum foil on ÄKTA pure FPLC system and run at a flow rate of 0.5 ml/min. To obtain the elution profile for the illuminated condition, protein samples collected from the peak fractions of the dark run were concentrated to 3 mg/ml (500 ml) and then pre-illuminated at 750 ± 10 nm filtered light for ~30 min before loading onto the same SEC column. The light run was carried out under the same condition as the dark run, except that white light was applied to the column throughout the light run.

Supplementary Discussion

Global kinetic analysis of the data from time-series 1 and 2

The global kinetic analysis for each dataset confirmed that merging the two datasets would not distort the results of the kinetic analysis. The results of the global kinetic analysis for the dataset of each time series are shown in fig. S4. By fitting the RSVs scaled with singular values, time constants of $80 (\pm 36) \mu\text{s}$ and $35 (\pm 102) \text{ms}$ were determined from the data of time series 1 (fig. S4, A to F) and time series 2 (fig. S4, G to L), respectively. The time constants of $80 \mu\text{s}$ and 35ms are highly similar to the time constants of $95 \mu\text{s}$ and 21ms , respectively, as determined from the fitting of the RSVs from the merged data. In the principal component analysis, the SADSs for both datasets were also calculated, and the SADS2 of time-series 1 showed good agreement with the SADS1 of time-series 2, indicating a high consistency between the two different data sets (fig. S4M). The high similarity between the time constants, and the coincidence of the SADS2 of time-series 1 and the SADS1 of time-series 2 guarantee that merging the two datasets did not cause any distortion in the results of the global kinetic analysis.

Static light-induced difference signals

SVD analysis of the measured static scattering curves of PaBphP revealed a major component attributed to the light-induced global structural changes between the dark-adapted and illuminated states. Specifically, the major component in terms of the scattering curves obtained from the SVD analysis features a positive amplitude below $q < 0.06 \text{ \AA}^{-1}$ and a negative scattering shape in the range of $0.06 \text{ \AA}^{-1} < q < 0.2 \text{ \AA}^{-1}$ (fig. S3B). The first right singular vector (RSV1) shows that these difference signals arise from light responses and are fully reversible, depending on the light conditions (fig. S3C). To explore these global protein structural changes, we directly compared the SVD-decomposed static difference curve, which is the first left singular vector (LSV1), with the difference scattering curve from a previously reported study of canonical DrBphP (fig. S3B). In the range of $0.03 \text{ \AA}^{-1} < q < 0.2 \text{ \AA}^{-1}$, the static difference curve for PaBphP shows noticeable discrepancy with that from the canonical DrBphP (ref. 8 of the main text). Based on these analyses, we speculate that the protein conformational changes involved in the light-induced transition of PaBphP are not identical to the structural changes observed in canonical DrBphP, although they may share similarities at the mechanistic level.

Effects of α -helix to β -sheet transitions in PHY arms on structural analysis

Previous structural studies have shown that the PHY arms of BphPs undergo a local structural change between the α -helix of Pfr and the β -sheet of Pr in the early stages of photo-induced transition (ref. 8, 22, 45 of the main text). This local structural change is presumed to act as a driving force for the global conformational changes of BphPs by inducing strain at the dimeric interface between the PHY domains. We investigated how local structural changes in the PHY arms affected our structural analysis. To this end, the α -helix PHY arms of the structure for I₂ that best describes the TRXSS data were replaced with the β -sheet PHY arms from the structure of DrBphP in the Pr state (ref. 8, 42 of the main text) (PDB ID: 4O0P) (fig. S6, A and B). The difference scattering curve was calculated using the resulting structure and compared to the original difference curve. The same type of simulation was performed for the protein structure of P. The replacement of α -helix PHY arms with β -sheet PHY arms did not significantly change the difference scattering curve, implying that such subtle changes in secondary structures would not be detectable in the current signal-to-noise ratio (SNR) (fig. S6, C and D).

Effect of helical distortion in MD-generated structures for the Pr state on structural analysis

In some of the MD-generated structures for the Pr state, helical distortions were observed near the Arg321 residues. The helical distortion originates from the difference in the degree of pulling at the two positions (Arg321s and Ala332s), where external forces are applied during the MD simulations. To investigate the effect of helical distortion on the structural analysis, we chose MD-sampled structures with and without helical distortion. From these structures, the theoretical difference curves were calculated using the same Pfr structure as a reference and compared with the experimental results. A comparison of the theoretical scattering curves shows that the occurrence of helical distortion causes an insignificant change in the scattering curve, which is indistinguishable within our experimental uncertainty (fig. S8).

Benchmark test for the calculation of a theoretical scattering curve

For the structural analysis, the theoretical scattering curves for the MD-generated structures were calculated using the CRY SOL program (ref. 60 of the main text) in the q -range corresponding to the experimental data. The electron density of the solvent was set to $0.334 \text{ e}/\text{\AA}^3$, corresponding to the environment of neat water, by considering the low-salt conditions in the buffer solution. The contrast of the hydration shell layer was set as $0.03 \text{ e}/\text{\AA}^3$. The maximum order of harmonics, which defines the resolution in the scattering curve, was set to a maximum value of 50, and the Fibonacci grid was set to a maximum value of 18. The other parameters of CRY SOL were set to default values. To check the effect of the hydration shell contrast used in CRY SOL, we performed an additional analysis of the static scattering curve with the dark-adapted state of PaBphP by changing the value of the shell contrast. The theoretical static scattering curves, calculated from the use of 0.02 and 0.04 $\text{e}/\text{\AA}^3$ in the shell contrast, show a prominent discrepancy from the experimental data, whereas the theoretical static scattering curve obtained using 0.03 $\text{e}/\text{\AA}^3$ in the shell contrast shows good agreement with the experimental data (fig. S9A). The results of the benchmark analysis of the static scattering curve indicate that it is reasonable to use default parameters for the calculations of the theoretical scattering curves in CRY SOL. We also conducted an additional test to check the accuracy of the theoretical scattering profile by comparing the results from CRY SOL, using the envelope function, and FoXs program, using the Debye equation. The theoretical difference scattering curves, calculated from the same structural coordinates with CRY SOL and FoXs, show almost identical features: thus, the difference between them can be indistinguishable within the

experimental error (fig. S9B). These results support that for the protein structures used in the structural analysis, the CRY SOL and FoXs programs provide the almost same accuracy in terms of the theoretical scattering profile.

Effective photoreaction yield of PaBphP

A scaling factor (μ), denoted in equation (2), consists of two parameters: (i) the relative ratio between the theoretical and experimental scattering curves, and (ii) the effective photoreaction yield, which depends on the primary quantum yield of PaBphP. Based on these parameters, the scaling factor can be calculated by multiplying the inverse value of (i) by the value of (ii). Based on the scaling factor used in the structural analysis, we estimated the effective photoreaction yield of PaBphP in the TRXSS measurement by considering the relative ratio between the “theoretical static” curve and the “experimental static” scattering curve for the dark-adapted PaBphP. From this estimation, the photoreaction yield was determined to be 0.3% ($\pm 0.015\%$). According to a nanosecond spectroscopic study (ref. 44 of the main text), it was reported that the photocycle of PaBphP initiated from the Pfr state accompanies a photoconversion yield of approximately 6%, which is 20 times greater than that estimated in our study. In general, the photoreaction yield is highly dependent on many experimental factors, including the existence of a ground-state-intermediate (GSI), sample concentration, temporal width, fluence, and the spot size of the pump laser pulse. In particular, the existence of a GSI formed in the ultrafast regime might induce a deactivation pathway, acting as a detour for the recovery of the ground-state population: thus, our result with the picosecond pump pulse seems to imply the existence of various deactivation pathways from the excited Pfr state.

Structural analysis of dark-adapted static scattering curve

Unlike in the crystal phase, it cannot be ruled out that PaBphP can exist as either a dimer or monomer of Pfr and Pr states in the solution phase. In this regard, we analyzed the dark-adapted static scattering curve of PaBphP to investigate the existence of PaBphP conformers in the solution phase. To this end, we used the structures of dimers for the dark-adapted Pfr and photoproduct Pr states obtained from the structural analysis shown in Fig. 3C and F, and the structures of the monomers were adopted from half of the dimer. Theoretical static scattering curves were calculated from the structures of dimers and monomers and were used to describe the experimental curves. The fractions of monomers, dimer Pfr, and dimer Pr were fitted until the theoretical scattering curve agreed well with the experimental curve. The ratio of PaBphP present as dimers to PaBphP present as monomers was determined to be about 100 (± 1.7):117 (± 0.4) (fig. S10A), and the ratio of Pfr to Pr in PaBphP present as dimers was 82 (± 1.3):18 (± 1.1) (fig. S10B). In other words, the analysis results show that the Pfr of PaBphP present as dimers and is predominant over Pr, which is consistent with our experimental conditions in which illumination was employed to make Pfr dominant.

As discussed in the main text, the TRXSS data were consistent with transitions involving only dimeric forms. On the other hand, the results from the structural analysis of the static X-ray scattering data show that dark-adapted PaBphP can exist in the monomeric form as well as in the dimeric form. Thus, we also checked whether monomer-related transitions could contribute to the TRXSS data. To quantitatively consider the effect of monomer-related transitions in the difference scattering curve, we performed an additional structural analysis based on the modeled structures of the dimeric and monomeric forms. For this purpose, we considered monomer-related transitions including monomer-to-monomer, monomer-to-dimer, dimer-to-monomer, and dimer-to-dimer

transitions (fig. S10). For each state (I₂ or P), the monomer units for these monomer-related transitions were constructed from one-half of the optimized dimeric structure determined from the structural analysis of the TRXSS data and one-half of the dimeric Pfr structure, corresponding to the initial state. The theoretical difference scattering curves for the dimer-to-dimer transition are in good agreement with the experimental data. In contrast, the amplitudes of the theoretical scattering curves for the monomer-to-monomer transition are much smaller than those for the dimer-to-dimer transition and do not agree well with the experimental curves (SADS2 and SADS3), implying that the monomer-to-monomer transitions are not likely to affect the results from the analysis of the TRXSS data. The amplitudes of the theoretical scattering curves for the monomer-to-dimer transition are comparable to those for the dimer-to-dimer transition shown in fig. S10C and D, but the agreement with the experimental curves (SADS2 and SADS3) is not good. Similarly, the dimer-to-monomer transition does not provide satisfactory agreement with the experimental curves (SADS2 and SADS3).

SEC elution profiles measured with dark-incubated and illuminated treatments

The elution profiles of SEC measured with dark-incubated and illuminated treatments show a difference, which supports that PaBphP has a larger effective hydrodynamic radius in the illuminated state than in the dark-incubated state (fig. S3A). Nevertheless, the shift is mild for the following reasons. First, PaBphP exists as a mixture of dimers and monomers in a ratio of 100:117. The presence of monomers broadens the elution profile. Second, we estimated the extent of conformational changes occurring in the Pfr-to-P transition in terms of protein volume. Based on the optimal protein structures from the structural analysis, the protein volumes of Pfr with II-framed geometry and P with O-framed geometry were determined to be 180,233 Å³ and 184,021 Å³, respectively, indicating that the protein volume of P is larger by 2% than that of Pfr. The change in hydrodynamic radius observed in the SEC is consistent with the increase in protein volume, accompanying the change from the II-framed geometry in Pfr to the O-framed geometry in P observed by TRXSS, and the volume change of 2% estimated from the dimer structures seems to be linked to the mild chromatographic shift in the SEC.

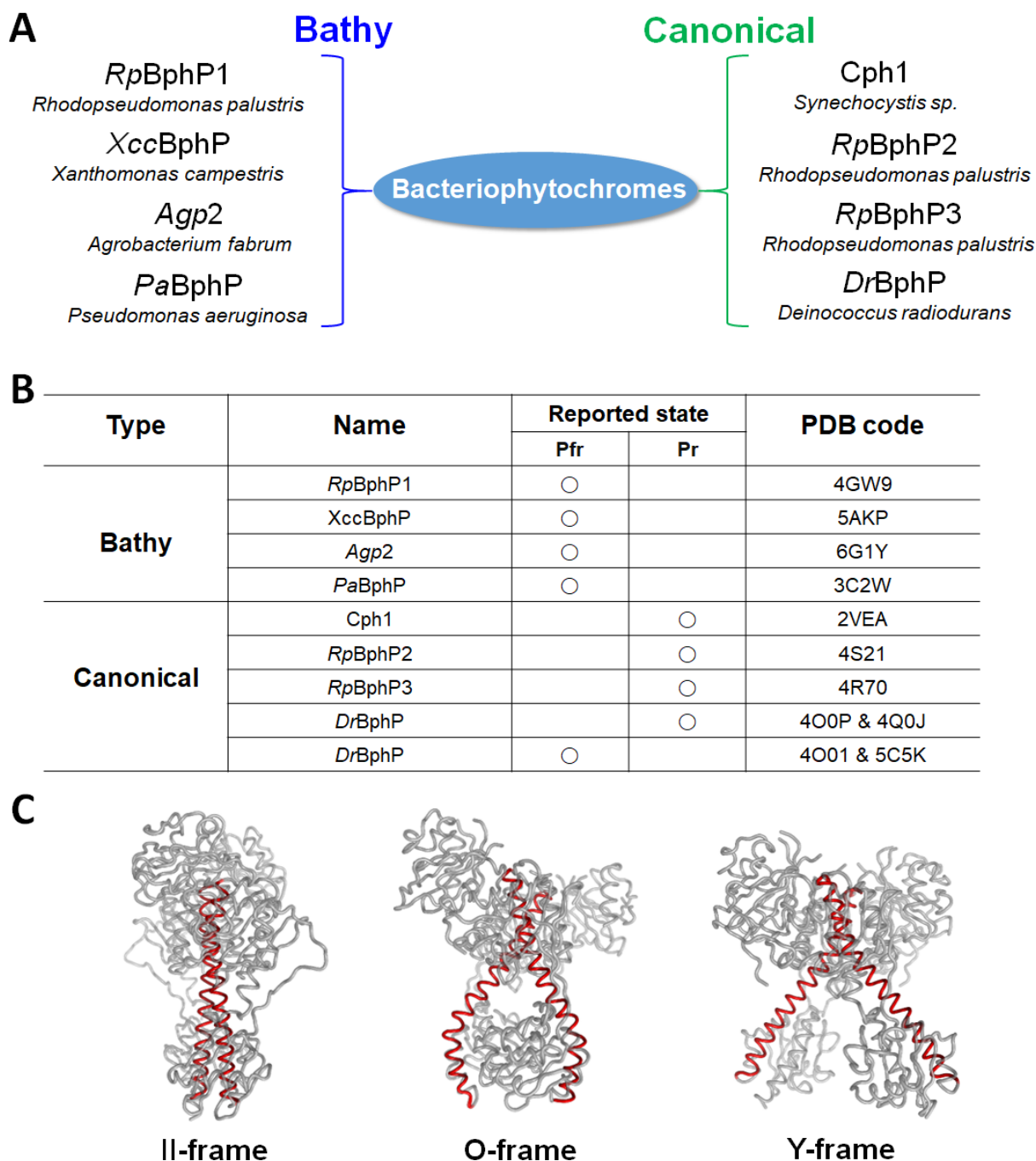


Fig. S1. Superfamily of bacteriophytochromes (BphPs). (A) BphP superfamily categorized as bathy or canonical forms. (B) Summary of the reported states of BphPs and crystallographic structures with PDB codes. Among the BphPs, the canonical DrBphP is the only case in which the protein structures for both the Pfr and Pr states have been reported. (C) Three different protein conformations for BphPs classified in terms of the geometry of the central helical backbones, (i) II-frame (left), (ii) O-frame (middle), (iii) Y-frame (right), based on the reported crystal structures of BphPs. For clarity, in each frame, the helical backbones are color-coded by red ribbons.

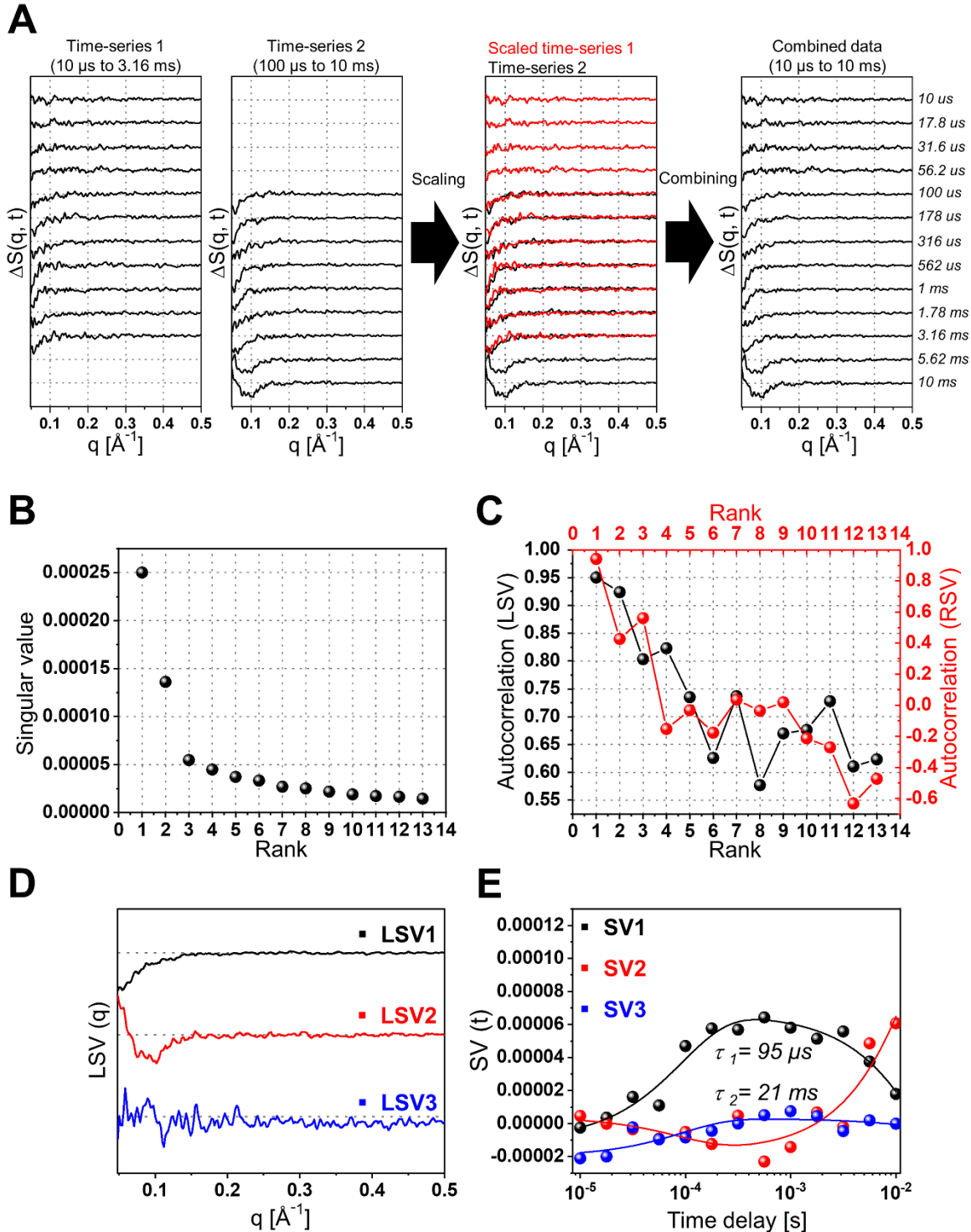


Fig. S2. SVD analysis of the combined time series of time-resolved X-ray scattering data. (A) Comparison of the data set in the time range from 10 μ s to 3.16 ms (time-series 1) with that in the time range from 100 μ s to 10 ms (time-series 2). The difference scattering curves at the shared time points between the first and second data sets were used to combine them. **(B - E)** Results from the SVD analysis of the merged data in the time range from 10 μ s to 10 ms. **(B)** Singular values (S). **(C)** Autocorrelation values of LSVs (black dots) and RSVs (red dots). **(D)** The three most

significant LSVs. **(E)** The three most significant RSVs multiplied by the corresponding singular values (S). The solid lines are the results from the exponential fitting with two common time constants; $95 (\pm 25) \mu\text{s}$ and $21 (\pm 32) \text{ms}$. Although the scattering feature of the third LSV (LSV3) is marginal compared to that of the other significant LSVs, the features of the third RSV seem to be meaningful. Considering the temporal feature of RSVs, at least the first three singular vectors are required to explain the kinetics in the time window from $10 \mu\text{s}$ to 10ms .

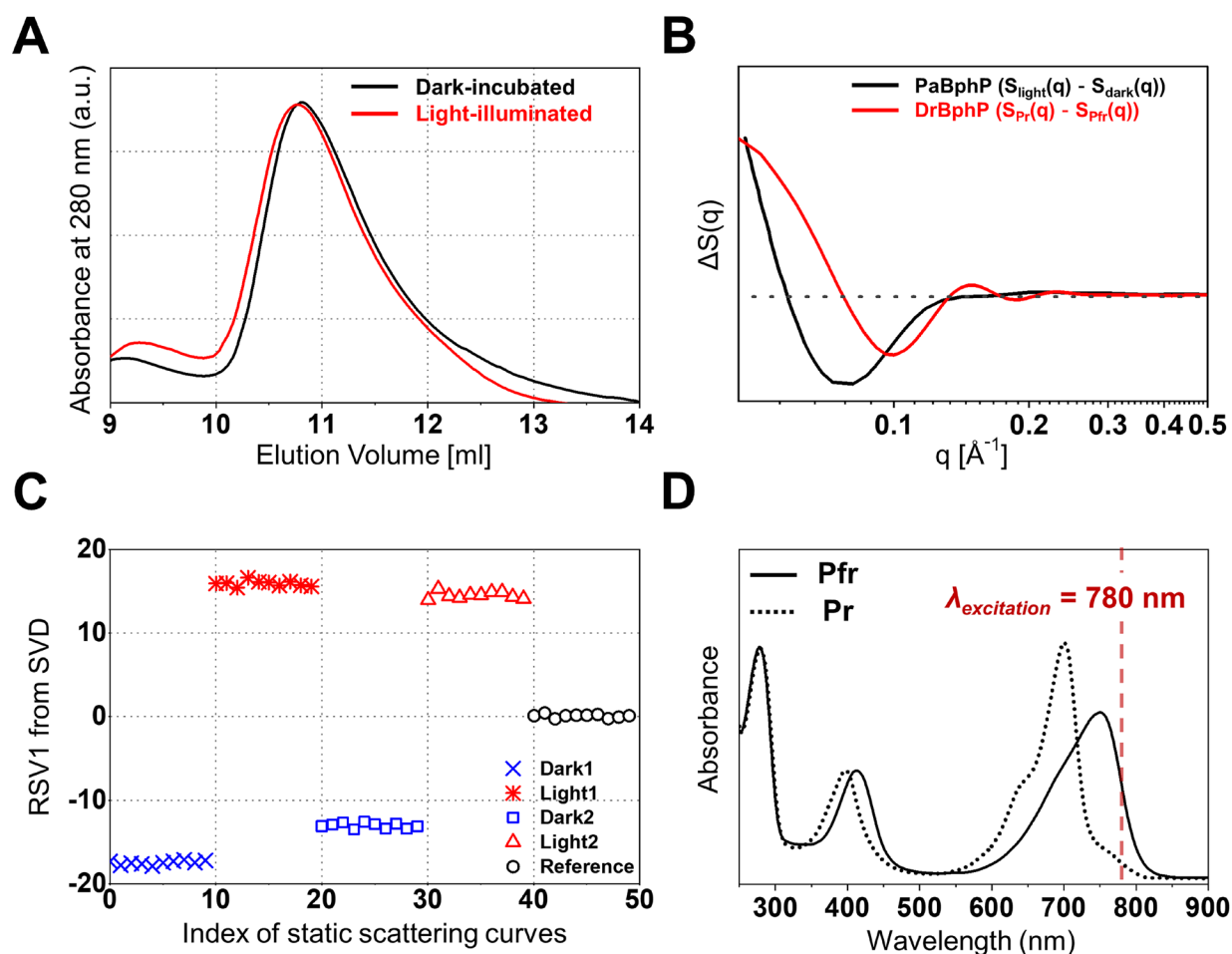


Fig. S3. Light-induced transitions of PaBphP in solution detected using size-exclusion chromatography (SEC), static X-ray solution scattering and UV-visible absorption spectroscopy. (A) SEC elution profiles of PaBphP obtained in the dark-incubated (black) and illuminated (red) conditions (see also Supplementary Materials). The SEC profiles show a light-induced shift suggesting a larger hydrodynamic molecular radius in the illuminated state. (B) Static difference scattering curves between Pr and Pfr states, $\Delta S_{\text{static}}(\text{Pr} - \text{Pfr})$. The static difference scattering curve for PaBphP (black) was obtained from the joint SVD analysis on a series of the static X-ray scattering curves measured using dark and illumination treatments. The experimental data for DrBphP (red) was adopted from the previously reported data (ref. 8 of the main text). (C) First right-singular vector (RSV1) from the SVD analysis on a series of static X-ray scattering curves. The static scattering curves were measured in two different conditions that alternated between the dark-incubated (blue symbols) and illuminated (red symbols) treatments twice. Subsequently, the reference scattering curves (black symbols) from the buffer alone were measured as the control experiment. A total of 50 static curves consisting of 20 curves were measured from the dark-incubation (Dark1 and Dark2), 20 curves from the illumination (Light1 and Light2), and 10 curves from the control. The amplitude changes in RSV1 show the reversible photoconversion between the dark-incubated (blue dots) and illuminated (red dots) states. (D) UV-visible absorption spectra of PaBphP in the Pfr (solid line) and Pr (dashed line) states. The red dashed line denotes the excitation wavelength (780 nm) used in this study, at which the Pfr state has significantly higher absorbance than the Pr state.

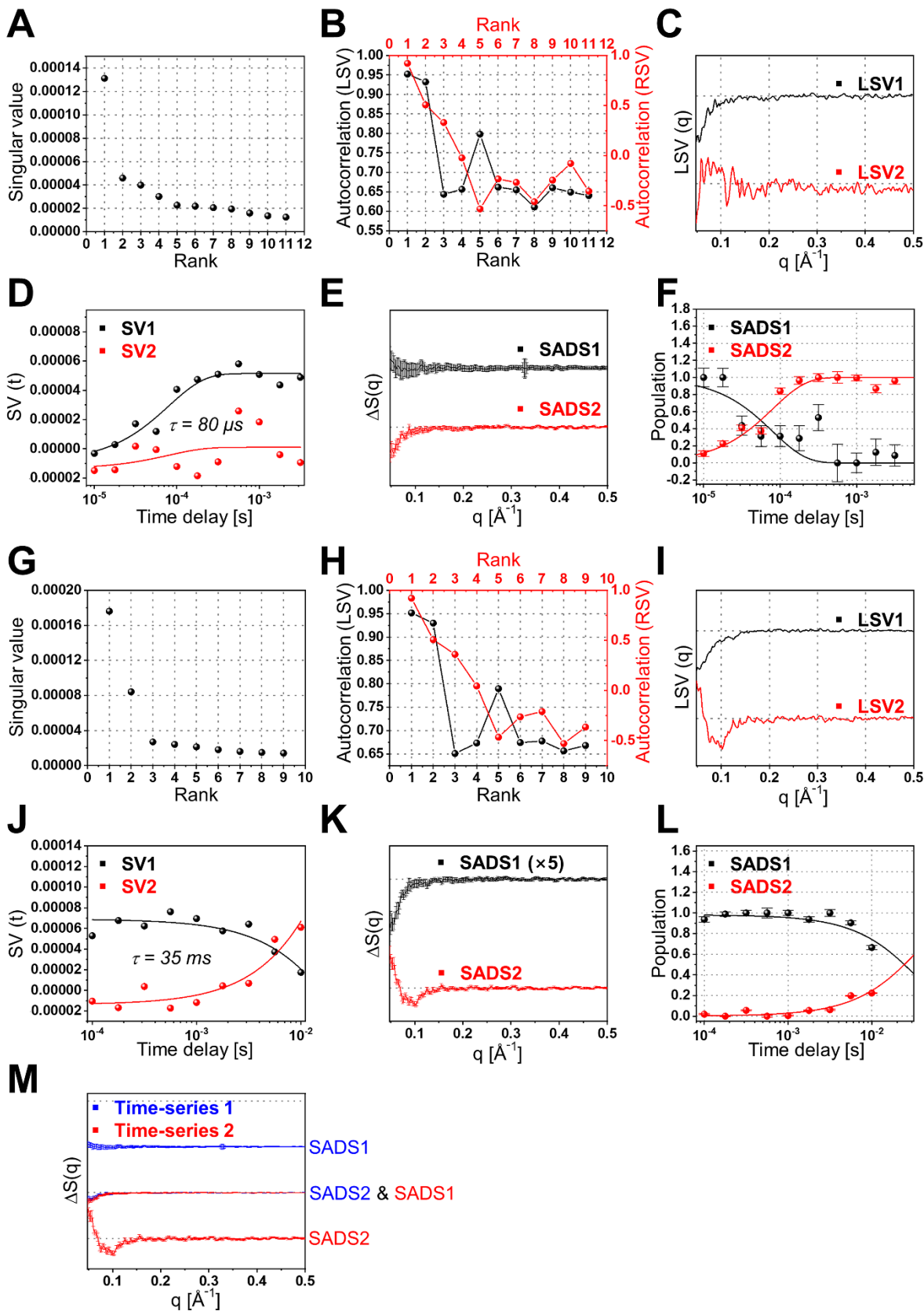
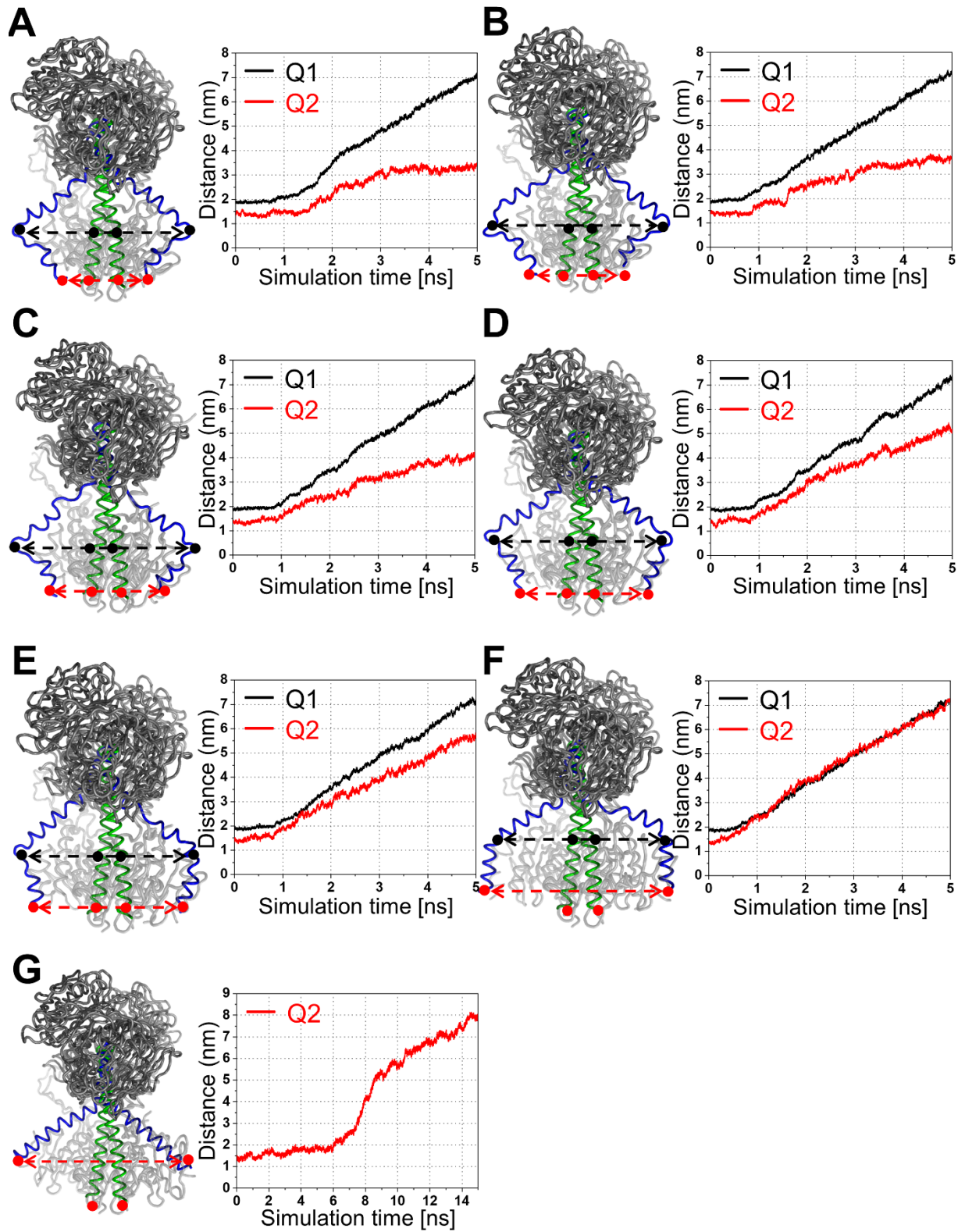


Fig. S4. Global kinetic analysis of the data sets from time-series 1 and 2. (A - F) Results from the global kinetic analysis of the data set of time-series 1 in the time range from 10 μs to 3.16 ms. (A) Singular values (S). (B) Autocorrelation values of LSVs (black dots) and RSVs (red dots). (C) The most significant LSVs. (D) The most significant RSVs multiplied by the corresponding singular values (S). The solid lines are the results from the exponential fitting with a common time constant of $80 (\pm 36) \mu\text{s}$. Considering the singular values, the features of singular vectors and their autocorrelation values, the first two LSVs and RSVs are sufficient to account for the data set of time-series 1. (E) Species-associated difference scattering curves (SADSs) from principal component analysis (PCA). (F) Time-dependent population changes. (G - L) Results from the global kinetic analysis of the data set from time-series 2 in the time range of 100 μs to 10 ms. (G) Singular values (S). (H) Autocorrelation values of LSVs (black dots) and RSVs (red dots). (I) The most significant LSVs. (J) The most significant RSVs multiplied by the corresponding singular values (S). The solid lines are the results from exponential fitting with a common time constant of $35 (\pm 102) \text{ms}$. Considering the singular values, the features of the singular vectors and their autocorrelation values, the first two LSVs and RSVs are sufficient to account for the data set. (K) SADSs from the PCA. (L) Time-dependent population changes. (M) Comparison of the SADSs from the kinetic analyses of the data from time-series 1 (blue) and time-series 2 (red). The SADS2 from time-series 1 shows good agreement with the SADS1 from the data of time-series 2, implying high consistency between the two different data sets.



• Arg321 • Ala332

Fig. S5. Protein conformers generated from the pulling simulation for the candidate structures with O- and Y-frames. (A - F) (Left) Protein structures for the initial and final states from the pulling simulation for the candidate structures with an O-frame. (Right) The profiles of the distance between two Arg321 (Q1) and the distance between two Ala332 (Q2) as a function of simulation time. The positions of Arg321s and Ala332s are denoted by the black and red dots, respectively. For the conformational diversity of simulated conformers in the pulling simulations, we performed six different pulling simulations starting from the same protein structure. In these simulations, Q1 was allowed to increase to ~ 7.0 nm, and Q2 to a value between ~ 3.0 nm and 7.0 nm. The helical backbones are represented with green (initial) and red (last) colors, respectively. Black and red dashed arrows show the pulling directions. (G) (Left) The initial structure with the II-frame is compared with the final structure with the Y-framed geometry, generated from the pulling simulation. For clarity, the helical backbones in the initial and final forms are color-coded in green and red. (Right) The profile of the distance between two Ala332 (Q2) as a function of simulation time during the pulling simulation for the candidate structures with Y-frames. The two Ala332 residues are denoted by red dots.

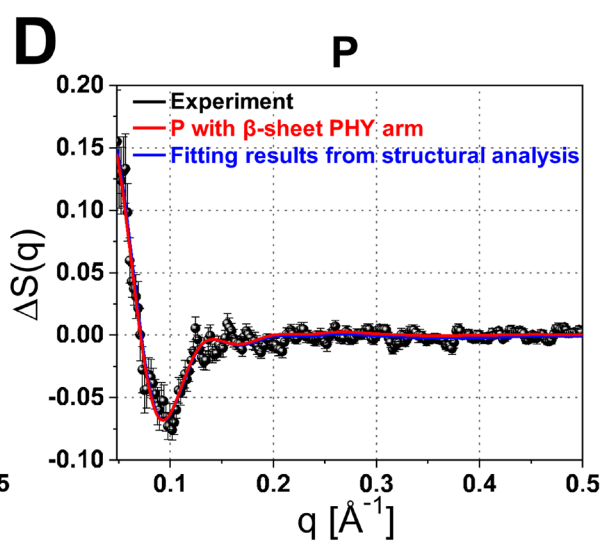
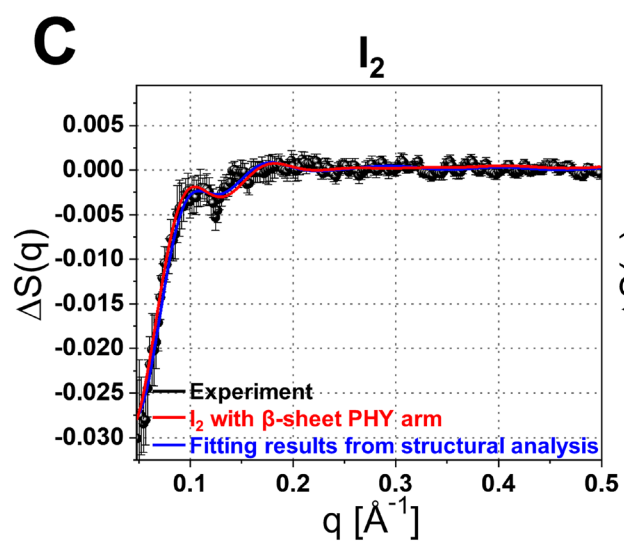
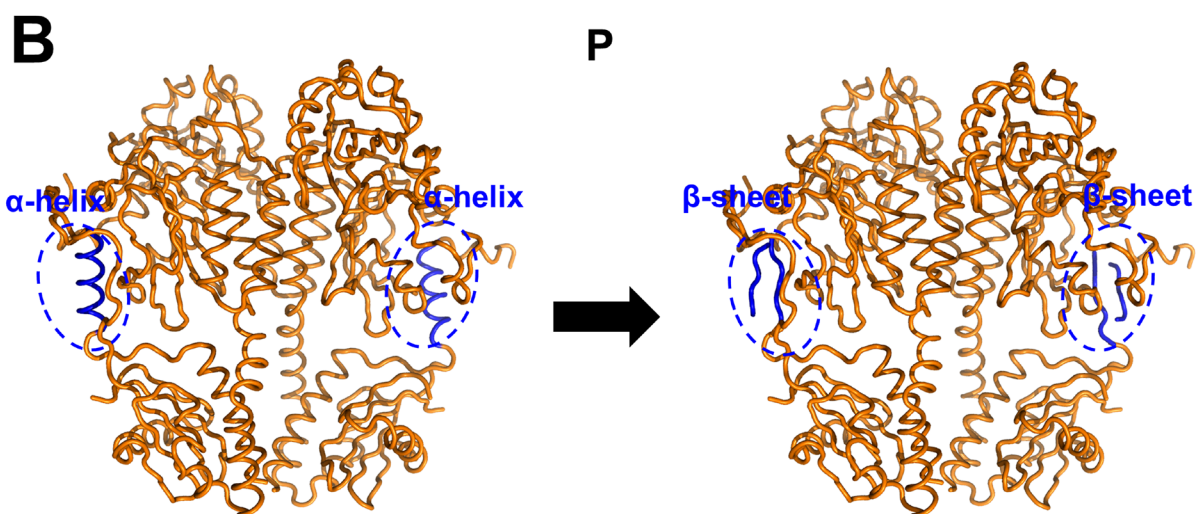
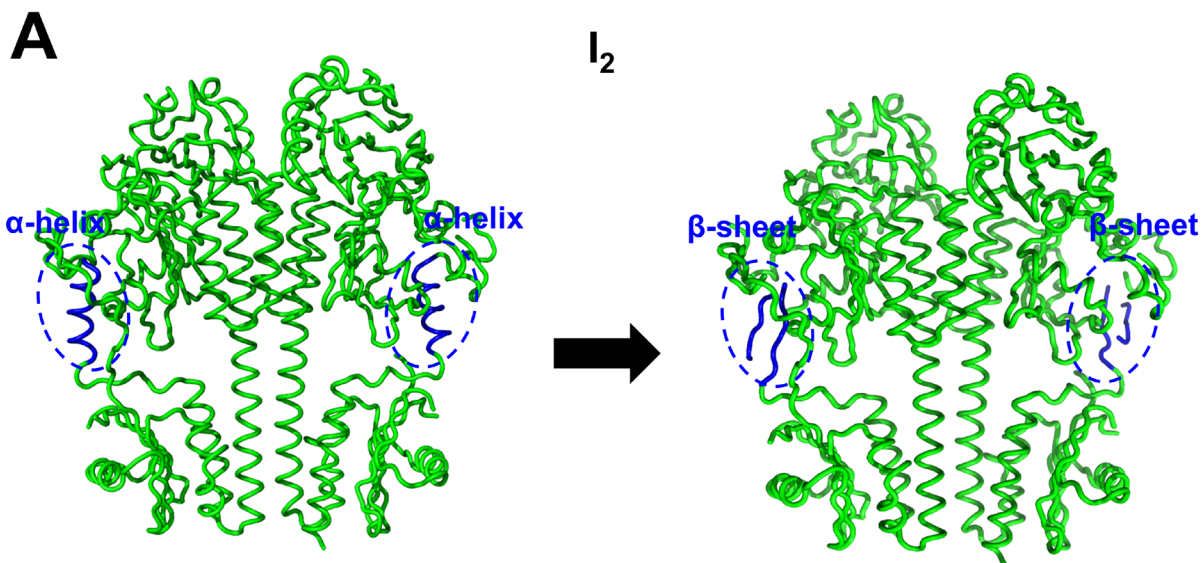


Fig. S6. Effect of the α -helix to β -sheet transition in the PHY arms of the difference scattering curve. (A, B) (Left) The optimal structures of I₂ (A) and P (B) that well describe the experimental data. (Right) To check how the α -helix to β -sheet transition around the PHY arms brings about the change in the difference scattering curve, we modeled the protein conformation based on the template structure of the Pr state in DrBphP (PDB ID: 4O0P). For clarity, the PHY arms are indicated with blue-colored residues. (C, D) Comparison of the difference scattering curves (blue) from the original optimal structures with α -helix around the PHY arms with those from the modeled structures with β -sheet around PHY arms (red) for SADS2 (left, black dots) and SADS3 (right, black dots). This comparison shows that the structural changes from the α -helix to β -sheet around the PHY arms are not detectable in the experimental data within the current SNR.

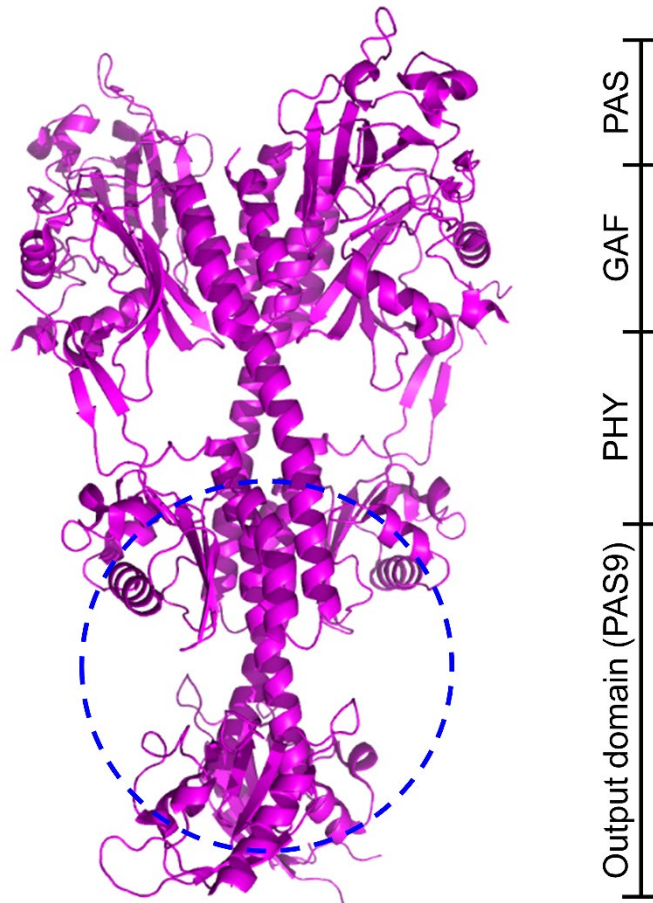


Fig. S7. Crystal structure for the Pr state of full-length XccBphP (PDB ID: 5AKP). Compared with the full-length structure of PaBphP, the structure of XccBphP has the PAS9 domain acting as the output domain. The helical backbones in the output domains of XccBphP, highlighted by a blue circle, are entangled with each other.

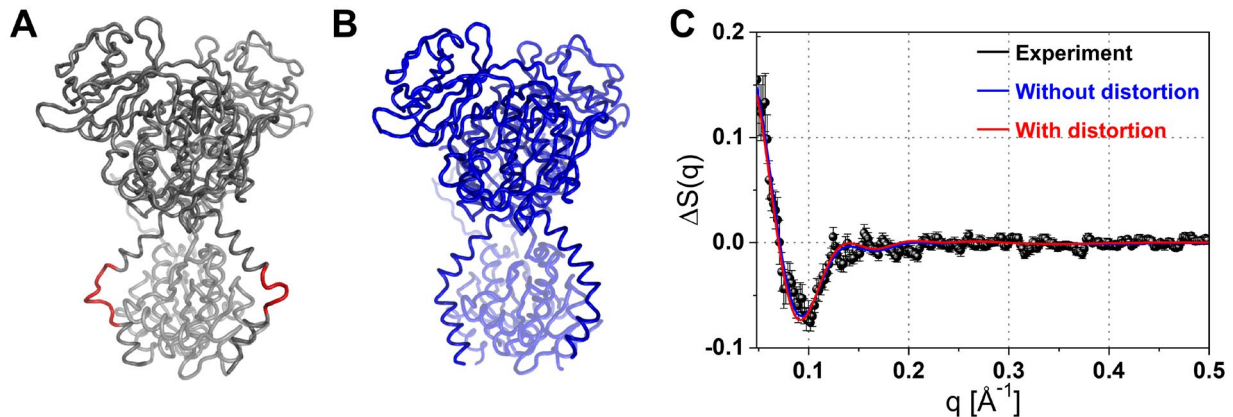


Fig. S8. Helical distortion in the structure of the photoproduct state from the structural analysis based on the MD simulations. (A) Representative MD-simulated structure for the photoproduct P state with helical distortion. This structure shows that the helical distortion occurs in the vicinity of the Arg321 residue. This structural distortion originates from the difference in the degree of pulling at the two positions (Arg321s and Ala332s) where the external forces are applied during the MD simulations. The distorted residues around the Arg321 residues are colored in red. (B) Representative MD-simulated structure for the P state without the helical distortion. This structure has a global shape that is highly similar to (A) without any structural distortion of the helical backbones around the Arg321 residues. (C) Comparison of the theoretical difference curves of (A) (red) and (B) (blue) using the same dark-adapted Pfr structure as the reference. This comparison shows that the existence of helical distortion hardly affects the difference scattering curve.

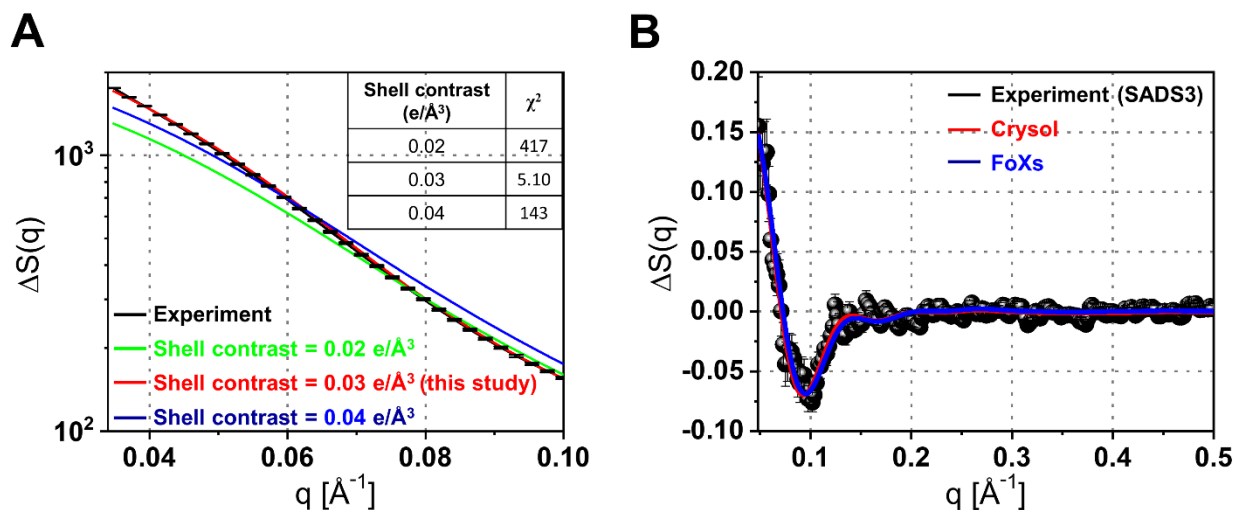


Fig. S9. Benchmark analysis for calculating theoretical X-ray scattering curves using CRY SOL and FoXs. (A) Effect of the hydration shell contrast on the analysis of the experimental static scattering curve for the dark-adapted PaBphP. In the range of $0.034 \text{ \AA}^{-1} < q < 0.1 \text{ \AA}^{-1}$, the experimental static curve (black) was compared with theoretical curves. For the theoretical curves, three different values of the hydration shell contrast were applied during the calculation using CRY SOL; (i) 0.02 e/\AA^3 (green), (ii) 0.03 e/\AA^3 (red), which is the default condition used in the analysis of all data in this study, and (iii) 0.04 e/\AA^3 (blue). Each theoretical static curve was obtained by fitting the relative population ratio for dimeric and monomeric structures in the same way as that of fig. S10A. The inset table shows the χ^2 value between the theoretical curve for each shell contrast and the experimental static curve. The theoretical curve to which 0.03 e/\AA^3 is applied (red) shows the same features as the experimental curve (black) within the experimental error, while the other two curves show noticeable discrepancies to the experimental curve. (B) Comparison of SADS3 (black dot) and two theoretical difference scattering curves calculated with CRY SOL (red) and FoXs program (blue). For the calculations of scattering curves, the protein structures of the photoproduct Pr state with an “O”-framed helical backbones and the initial Pfr state with the parallel helical backbones (II-frame) were used. Both theoretical difference curves show good agreement with SADS3 within the experimental error of SADS3.

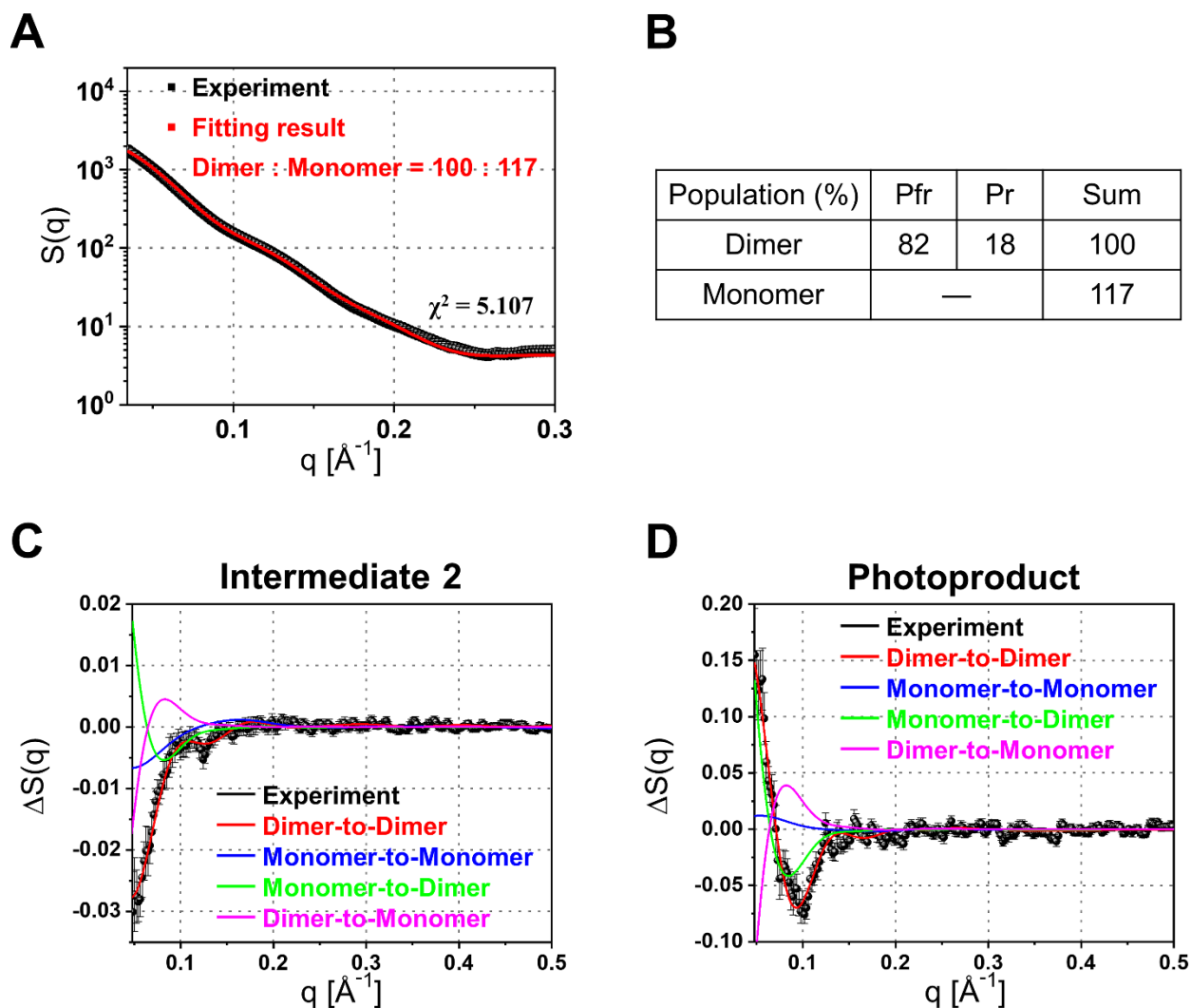


Fig. S10. Analyses of the static scattering curve for the dark-adapted PaBphP and the consideration of possible monomer-related transitions in the difference curves. **(A)** Comparison between the experimental (black dot) and theoretical (red line) static curves for the dark-adapted static scattering curve of PaBphP. The theoretical scattering curve was obtained by fitting the relative population of the dimeric and monomeric PaBphP based on the structures of the ground-state Pfr and the photoproduct Pr determined from TRXSS. With the ratios summarized in **(B)**, the theoretical scattering curve shows excellent agreement with the experimental one. **(B)** Summary of the population ratio between Pfr and Pr in the dimeric form and the population ratio between monomeric and dimeric forms determined from the fitting. These ratios determined from least-squares fitting of the dark-adapted static scattering curve shown in **(A)** are $\sim 100:117$ between the dimeric and monomeric forms and $\sim 82:18$ between Pfr and Pr of the dimeric form, respectively. The monomer could not be categorized by the types of Pfr and Pr states. Instead, the total population of the monomeric form was determined to be 117% relative to the dimeric form (set at the 100% population). **(C)** Comparison of SADS2 (black dot; corresponding to I_2) and the difference curves calculated for various structural transitions. **(D)** Comparison of SADS3 (black dot; corresponding to P) and the theoretical difference curves for the three different structural transitions. In **(C)** and **(D)**, the theoretical difference scattering curves (colored lines) were

generated by considering the four different situations; (i) dimer-to-dimer transition (red), (ii) monomer-to-monomer transition (blue), (iii) monomer-to-dimer transition (green), and (iv) dimer-to-monomer transition (magenta). In terms of the similarity between the profiles, the theoretical curves associated with the dimer-to-dimer transitions (red line) are in good agreement with SADSs (black dot) in both (C) and (D).